Journal of Dynamics, Monitoring and Diagnostics, 2026, 5, 38-48
https://doi.org/10.37965/jdmd.2026.792

ISTP
RESEARCH ARTICLE

Real-Time Monitoring of Clump Weight Integrity Loss in Floating Wind Turbines via Deep Learning

Adarsh Arya,[1] Rohit Kumar,[1] Arvind Keprate,[2] and Subhamoy Sen[1]
[1]i4S Laboratory, Indian Institute of Technology Mandi, Mandi, HP, India
[2]Green Energy Lab, Department of Mechanical, Electrical and Chemical Engineering, Oslo Metropolitan University, Oslo, Norway

(Received 21 April 2025; Revised 17 September 2025; Accepted 18 November 2025; Published online 18 November 2025)

Abstract: Floating offshore wind turbines (FOWTs) represent a promising avenue for harnessing wind energy in deep-water regions through the use of mooring systems. However, mooring lines account for over 20% of the total construction cost and require careful optimization to ensure both structural stability and economic feasibility. One effective strategy for enhancing mooring performance is the strategic placement of clump weights along the lines. While beneficial, these clump weights are vulnerable to damage or detachment under harsh marine conditions, potentially compromising the structural integrity and reducing the service life of FOWTs. To address this challenge, we propose a deep learning-based method for real-time detection of clump weight loss using a long short-term memory (LSTM) network. The training data for the LSTM model are generated using high-fidelity simulations conducted in the open-source software OpenFAST, based on the 5 MW OC3-Hywind spar-buoy FOWT model equipped with clump-weighted mooring lines. The proposed LSTM classifier achieved 86% accuracy on a held-out test split and 73% on a completely unseen dataset, demonstrating both effectiveness in detecting clump weight loss and generalization capability for real-time condition monitoring in FOWT mooring systems.

Keywords: clump weights; deep learning; FOWT; LSTM; mooring lines

I. INTRODUCTION

Floating offshore wind turbines (FOWTs) have emerged as a promising technology for harnessing wind energy in deep-water regions, enabled by mooring systems where the installation of conventional fixed-bottom turbines is technically and economically unfeasible. The ability of FOWTs to access stronger and more consistent wind resources makes them a key enabler in the transition to low-carbon, sustainable energy systems. Despite their promise, the widespread adoption of FOWTs remains constrained by high capital and operational costs. Achieving cost-competitiveness with traditional energy sources necessitates innovative design and engineering solutions that can improve performance while reducing expenses, with particular attention to the mooring system, which alone contributes over 20% of the total construction cost [1].

Mooring lines are essential for maintaining the station-keeping ability of floating platforms by resisting environmental forces such as wind, waves, and ocean currents. These forces can induce significant dynamic loads, leading to excessive tension in the mooring lines [2]. Industrial surveys highlight the mooring system as a critical and failure-prone component of FOWTs [3,4]. Typically constructed partially or entirely from steel, mooring lines are susceptible to degradation from corrosion and fatigue over time. This degradation can reduce line weight and pretension, increasing the likelihood of excessive tension failures or premature fatigue damage. In severe conditions, such failures may place the structural integrity of the entire FOWT system in danger [5]. Clump weights—discrete masses strategically attached along the mooring lines—have been increasingly implemented in FOWT designs to enhance mooring system reliability and performance [6–9]. These studies have demonstrated their effectiveness in mitigating platform motion, particularly in surge. Pan *et al.* reported up to 14% material savings in the mooring system using 40-ton clump weights [9]. Under extreme weather conditions, Li *et al.* showed that 100-ton weights outperformed heavy chains in reducing surge and stabilizing line tensions [7]. Ding *et al.* investigated weights from 5 to 65 tons placed at fixed locations and observed consistent improvements in motion mitigation with increasing mass [8]. Chen *et al.* addressed fatigue concerns, recommending a maximum of 60 tons to balance dynamic performance and fatigue life [10]. These variations reflect the influence of factors such as water depth, platform type, and mooring configuration. Overall, these weights improve the geometric stiffness of the mooring system, increase pretension, and effectively mitigate platform motions without requiring longer or more robust mooring lines.

In this study, we employ the widely used 5 MW OC3-Hywind FOWT model to explore a clump weight design space. Specifically, we analyze weights ranging from 0 to 60 tons (in 10-ton increments) positioned at 50–100 m intervals over the unstretched length of the mooring line.

However, clump weights are susceptible to uncertain movements due to harsh sea conditions. This continuous movement of clump weights and their connectors can lead to fatigue-related degradation and increase the risk of detachment over time [11,12]. Detachment caused by fatigue, corrosion, or extreme environmental conditions can result in increased platform motion, elevated mooring line tension, and, potentially, system failure. As highlighted

---

Corresponding author: Subhamoy Sen (e-mail: subhamoy@iitmandi.ac.in).

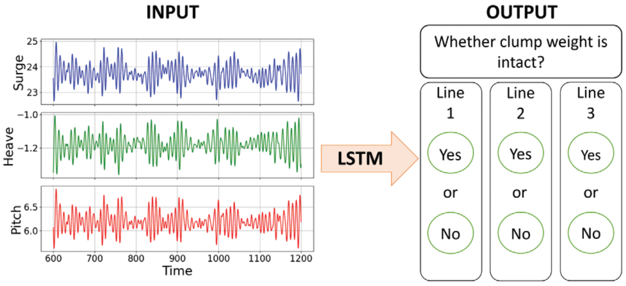

Fig. 1. Schematic illustration of the LSTM model's input–output relationship.

by Zhang and Wang, the sudden loss of a clump weight significantly alters the dynamic behavior and mechanical characteristics of the mooring system, compromising overall stability and potentially triggering structural failure [13]. This challenge is further intensified by the logistical difficulties of offshore inspections, where such failures may remain undetected until their consequences become critical [5,14].

Significant progress has been made in the detection of mooring failures in FOWTs. However, most existing studies have largely overlooked the role and potential failure of clump weights in mooring systems [15–17]. Despite the increasing deployment of FOWTs and their inherently complex dynamic behavior, there has been no dedicated investigation into damage detection specifically related to clump weights. This presents a clear gap in the literature and underscores the need for a targeted algorithm capable of addressing this critical aspect of mooring integrity.

Conventional damage detection techniques in FOWTs typically rely on structural health monitoring (SHM) approaches, including acoustic emission, visual inspection, and, more recently, machine learning (ML)-based methods [18–20]. Among these, deep learning (DL) techniques—particularly artificial neural networks (ANNs) and long short-term memory (LSTM) networks—have shown promising potential for real-time diagnostics by effectively capturing the complex temporal dynamics characteristic of FOWTs [17,21,22].

DL models have shown strong potential not only for damage detection but also for damage classification, including architectures such as LSTMs, gated recurrent units (GRUs), and transformers [23,24]. Hybrid architectures, such as self-attention-enhanced LSTMs, have demonstrated substantial improvements in classification accuracy [25]. These DL frameworks have been successfully applied to damage detection tasks in offshore wind turbines; for example, GRU-based models have achieved high accuracy in detecting blade damage [26].

However, these high-accuracy models typically rely on direct sensor measurements, which can be costly or impractical for underwater components such as clump weights. Consequently, many studies advocate for indirect sensing approaches, and in such contexts, LSTMs have proven effective in interpreting indirect responses for classification tasks [27,28]. Building on this insight, we propose a novel LSTM-based data-driven framework to detect clump weight loss in FOWT mooring systems. The framework leverages an LSTM-based diagnostic model trained to recognize various failure scenarios by analyzing platform motion responses that are sensitive to clump weight loss. The trained model classifies whether the clump weight is intact or missing, offering a scalable, real-time alternative to conventional inspection methods and enhancing the operational reliability of floating wind systems. To meet the data demands of the DL model, simulation datasets are generated using the open-source software OpenFAST. The overall input–output relationship of the proposed framework is illustrated in Fig. 1.

The rest of the paper is structured as follows: Section II introduces the OC3 FOWT model along with the integration of clump weights into the mooring system design. Section III details the LSTM-based diagnostic framework developed for clump weight loss detection. Section IV details the clump weight loss detection study, including input feature selection, simulation setup, and LSTM training. Section V discusses the key findings and limitations of the proposed approach. Finally, Section VI concludes the study with a summary of contributions and directions for future work.

II. FOWT SIMULATION MODEL

This study employs the OC3-Hywind spar-buoy FOWT model developed by the National Renewable Energy Laboratory (NREL) [29]. The spar buoy configuration is one of the most widely adopted designs for FOWTs due to its excellent stability characteristics and suitability for deep-water installations [6].

Details of the OC3-Hywind model are provided in Table I, and a schematic front view is illustrated in Fig. 2. The platform is anchored using three catenary mooring lines arranged at 120° intervals, as depicted in the top-view schematic in Fig. 3. The anchor and fairlead coordinates of the three mooring lines are listed in Table II. These coordinates define the baseline geometry of the OC3-Hywind spar mooring system and were directly used in all subsequent OpenFAST simulations.

The model is simulated using the open-source software OpenFAST, developed by the NREL [30]. OpenFAST integrates various physics-based modules to simulate the coupled dynamics of FOWTs. The AeroDyn module handles the aerodynamic loading on the rotor blades due to

Table I. OC3-Hywind spar floating wind turbine properties (WL: water level)

Wind turbine	
Rated wind speed	11.4 m/s
Rotor diameter and hub height	126 m, 90 m
Blade length and tower height	61.5 m, 77.6 m
Tower top and tower bottom (above WL)	87.6 m, 10 m
Platform base (below WL)	120 m
Mooring system	
Water depth	320 m
Catenary mooring lines	3
Mooring diameter	0.09 m
Mass density	77.71 kg/m
Axial stiffness	384.243 MN
Unstretched length	902.2 m
Fairleads depth (below WL)	70 m

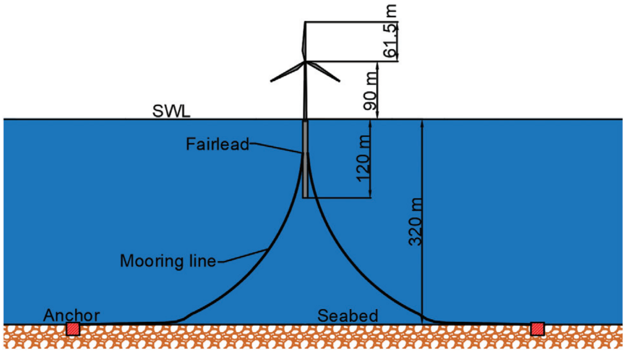

Fig. 2. Front view schematic of OC3-Hywind spar platform.

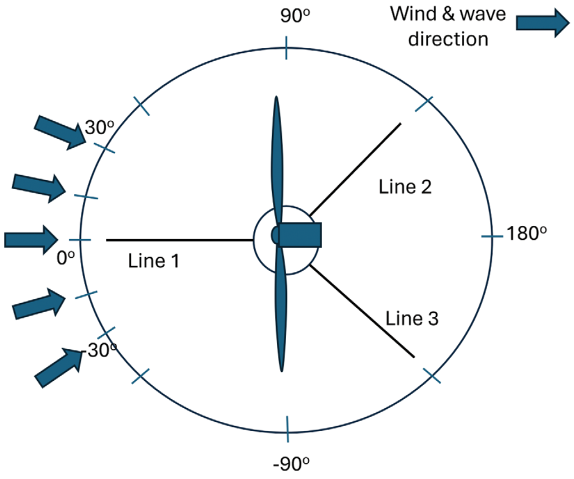

Fig. 3. Top view of OC3-Hywind spar platform with wind and wave direction.

Table II. OC3-Hywind spar mooring line connection coordinates

Mooring line	Connection	X (m)	Y (m)	Z (m)
1	Anchor	853.87	0.00	−320.00
	Fairlead	5.20	0.00	−70.00
2	Anchor	−426.94	739.47	−320.00
	Fairlead	−2.60	4.50	−70.00
3	Anchor	−426.94	−739.47	−320.00
	Fairlead	−2.60	−4.50	−70.00

wind. The ElastoDyn module computes the structural dynamics of the turbine, including flexible deformations of the blades, tower, and drivetrain. For wave and current loading, the HydroDyn module implements linear potential flow theory and Morison's equation. The InflowWind module supplies environmental wind conditions based on user-defined profiles. MoorDyn is employed for modeling the dynamic behavior of the mooring system. It treats mooring lines as a series of lumped masses connected by elastic segments. In this study, clump weights were incorporated in MoorDyn to enhance platform stability and reduce surge motion [31]. The original positional coordinates of the catenary lines in the OC3 configuration are modified to insert the clump weights at varying distances from the fairlead (c.f. Fig. 5).

The dynamic behavior of the floating platform can be described by the following equation of motion [32]:

$$\mathbf{M}\ddot{\mathbf{x}}(t) + \mathbf{C}\dot{\mathbf{x}}(t) + \mathbf{K}\mathbf{x}(t) = \mathbf{F}_{\text{env}}(t) \tag{1}$$

where $\mathbf{M}$, $\mathbf{C}$, and $\mathbf{K}$ are the mass, damping, and stiffness matrices for six degrees of freedom (DOF) of the system, respectively; $\mathbf{x}(t)$, $\dot{\mathbf{x}}(t)$, and $\ddot{\mathbf{x}}(t)$ are the displacement, velocity, and acceleration vector, respectively; and $\mathbf{F}_{\text{env}}(t)$ represents the environmental forces induced by wind, waves, and currents.

The wave forces in the simulation are generated using Airy wave theory within the HydroDyn module of OpenFAST. The sea state is characterized using the JONSWAP (Joint North Sea Wave Project) spectrum, which defines wave energy distribution as a frequency function. The JONSWAP spectral density function is given by Hasselmann *et al.* [33]:

$$S(\omega) = \alpha g^2 \omega^{-5} \exp\left[-\frac{5}{4}\left(\frac{\omega_p}{\omega}\right)^4\right] \gamma^{\exp\left[-\frac{(\omega-\omega_p)^2}{2\sigma^2\omega_p^2}\right]} \tag{2}$$

where $S(\omega)$ is the spectral density, ω is the wave frequency, ω_p is the peak frequency, g is the gravitational acceleration, α is the Phillips constant, γ is the peak enhancement factor, and σ is the width parameter, typically taken as 0.07 for $\omega < \omega_p$ and 0.09 for $\omega > \omega_p$.

Wind forcing is introduced using the InflowWind module of OpenFAST, where a steady wind profile is defined using the power law for wind shear. This empirical relation accounts for the increase in wind speed with height above the mean sea level and is given by Burton *et al.* [34]:

$$U(z) = U_{\text{ref}} \left(\frac{z}{z_{\text{ref}}}\right)^{\alpha} \tag{3}$$

where $U(z)$ denotes the wind speed at height z, U_{ref} is the reference wind speed corresponding to the reference height z_{ref}, and α is the wind shear exponent.

To ensure the accuracy of the implemented OC3-Hywind spar-buoy model, free-decay simulations were conducted in OpenFAST to extract the system's natural frequencies. Each DOF—such as platform surge, heave, pitch, and yaw—was individually excited by applying small initial displacements for no wind and still water conditions. The resulting 500-second time series were analyzed to obtain dominant frequencies, which were then compared with reference values reported in the OC3 Phase IV benchmark study [35]. The comparison, summarized in Table III, shows strong agreement between the simulated and reported values, validating the correctness of the model configuration.

The hydrodynamic and structural modeling fidelity was further validated by computing the platform's response amplitude operator (RAO) for surge and pitch motions under wave-only excitation, following the approach suggested by Bruschi *et al.* [6]. The RAO provides critical insight into the system's hydrodynamic behavior and is defined as:

$$\text{RAO} = \frac{\text{Platform Motion Amplitude}}{\text{Wave Amplitude}}. \tag{4}$$

Table III. Natural frequencies validation of the OC3-Hywind model

Mode	This study	Jonkman and Musial [35]
Surge	0.008 Hz	0.008 Hz
Sway	0.008 Hz	0.008 Hz
Heave	0.032 Hz	0.032 Hz
Roll	0.034 Hz	0.034 Hz
Pitch	0.034 Hz	0.034 Hz
Yaw	0.130 Hz	0.130 Hz

As shown in Fig. 4, the simulated RAO responses for surge and pitch align closely with the results reported by Bruschi *et al.* [6]. Figs. 4a and 4b demonstrate the surge and pitch motion RAO validation. While wave-only conditions were used here for benchmarking, subsequent simulations incorporated in this study combined wind and wave loading to reflect realistic offshore environments.

Floating platforms are subject to six DOF, among which surge is typically the most dominant motion. The optimal placement of clump weights aims to minimize this surge motion. To investigate the effect of clump weight location, simulations were conducted by placing clump weights at nine different positions along the unstretched length of the mooring line (902.2 m), ranging from 100 to 700 meters from the fairlead. The specific locations considered are illustrated in Fig. 5. The clump weight mass was varied from 10 to 60 tons in increments of 10 tons. The clump weight mass was constrained to a maximum of 60 tons in this study, following the recommendations of Chen *et al.* [10], to maintain an effective balance between motion suppression and mooring line fatigue life. In OpenFAST, it is standard practice for all loads to be applied simultaneously, which typically results in an initial transient phase. However, since such transient behavior does not occur in real-world operations, we excluded the first 600 seconds of simulation data to eliminate its effects.

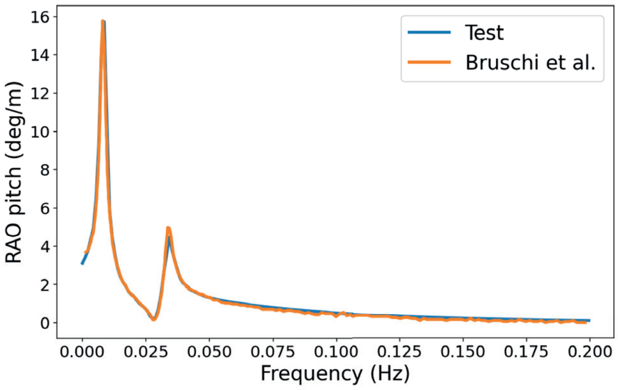

(a) Surge RAO comparison with Bruschi et al. [6].

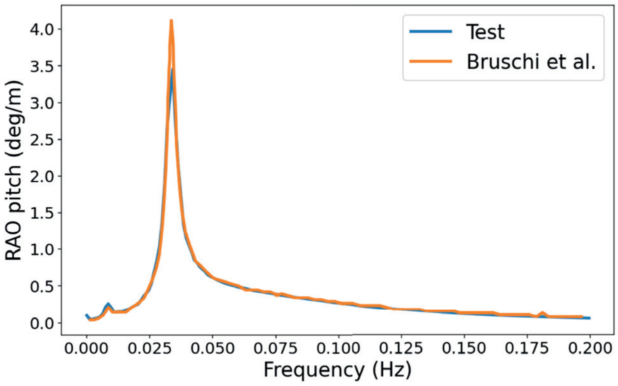

(b) Pitch RAO comparison with Bruschi et al. [6].

Fig. 4. Comparison of simulated RAOs with Bruschi *et al.* under wave-only excitation [6].

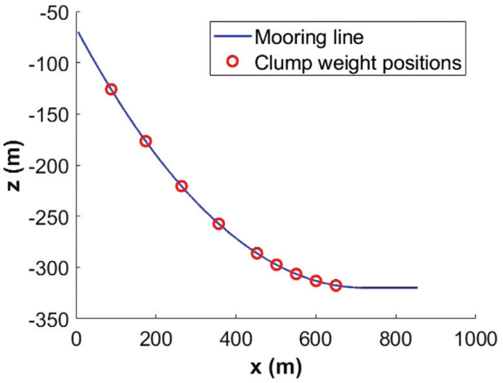

Fig. 5. Location of clump weights.

The primary objective of incorporating a clump weight in a mooring system is to reduce the dominant motions of the FOWT while minimizing the additional tension introduced in the mooring lines. To achieve this, two sets of studies were conducted. The first focused on positional analysis, aiming to identify the optimal placement of the clump weight along the unstretched length of the mooring line. The second investigated the optimal clump weight mass, determining the weight that yields the most favorable balance between motion reduction and tension control.

Heatmaps were generated to visualize the maximum surge motion and mooring line tension as functions of clump weight mass and position, providing a concise overview as shown in Fig. 6.

Based on the analyses—illustrated in Fig. 7a and the heatmap in Fig. 6a—surge motion was minimized when 60-ton clump weights were positioned between 500 and 600 meters, with optimal performance observed at 550 meters. This configuration also kept mooring line tension within acceptable limits, as demonstrated in Fig. 7b and the corresponding tension heatmap (cf. Fig. 6b).

A 3D surface plot (Fig. 8) further elucidates the trade-off between surge reduction and tension increase. The configuration of a 60-ton clump weight placed at 550 meters emerged as the most favorable solution, yielding the best compromise between surge suppression and line tension control. Quantitative comparisons further highlight the trade-offs observed in Figs. 5–7. The configuration with a 60-ton clump weight positioned at 550 m reduced the maximum surge response by nearly 50% compared to the baseline case without clump weights, while the corresponding increase in fairlead tension was limited to about 35%. By contrast, placing the same 60-ton weight at 300 m achieved only a 15% reduction in surge but led to an increase of nearly 60% in fairlead tension. These results demonstrate that the 550 m location offers the most effective balance between surge suppression and tension control, which is consistent with the optimal region identified in the heatmaps (Fig. 6) and the 3D surface plot (Fig. 8).

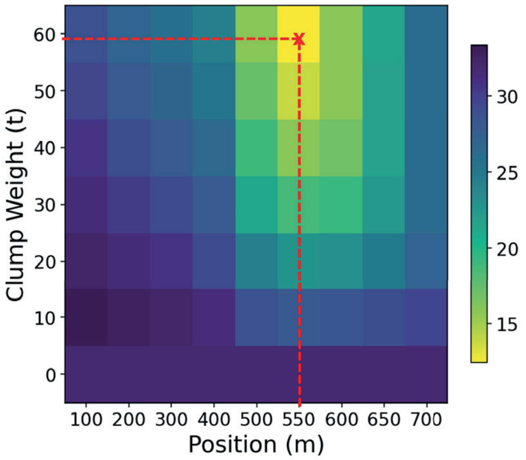

(a) Heatmap of maximum surge variation.

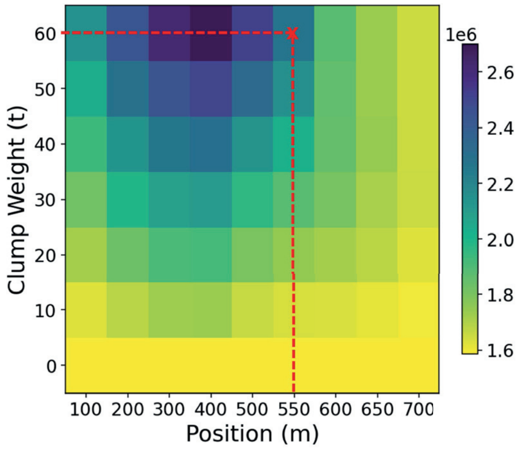

(b) Heatmap of maximum fairlead tension variation.

Fig. 6. Heatmaps for variations in surge and tension.

To enable real-time detection of clump weight loss, an LSTM-based framework is developed and trained using platform motion sensor data discussed in the next section, which is typically available in most FOWT systems. This approach facilitates accurate condition monitoring while minimizing the risk of system failure.

III. DATA-DRIVEN LSTM CLASSIFIER

LSTM networks are specifically designed to efficiently learn and retain long-range dependencies within sequential data [36]. They achieve this through a structured architecture composed of gates and memory cells, which control the flow and preservation of information over time (Fig. 9).

The forget gate $\mathbf{f}_t$ regulates how much of the previous memory cell $\mathbf{c}_{t-1}$ should be retained:

$$\mathbf{f}_t = \sigma(\mathbf{W}_f[\mathbf{h}_{t-1}\ \mathbf{x}_t] + \mathbf{b}_f) \tag{5}$$

where $\sigma(\cdot)$ is the sigmoid function, $\mathbf{W}_f$ is the weight matrix, and $\mathbf{b}_f$ is the corresponding bias vector for the forget gate. Next, the input gate, represented as $\mathbf{i}_t$, determines which portions of the new input should be written into the memory cell:

$$\mathbf{i}_t = \sigma(\mathbf{W}_i[\mathbf{h}_{t-1}\ \mathbf{x}_t] + \mathbf{b}_i) \tag{6}$$

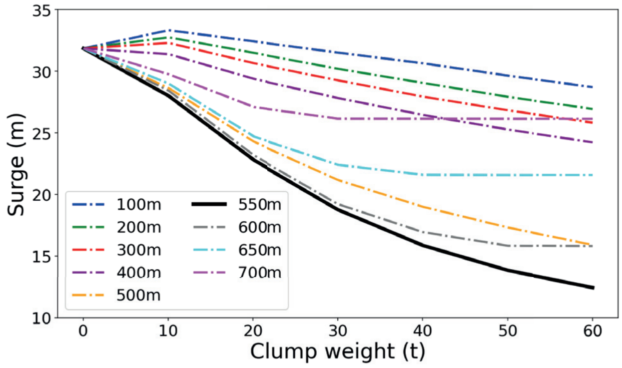

(a) Maximum surge variation.

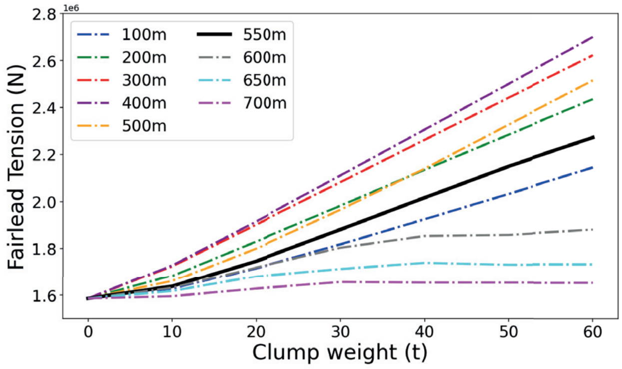

(b) Maximum fairlead tension variation.

Fig. 7. Variations of surge and tension for different clump weight positions.

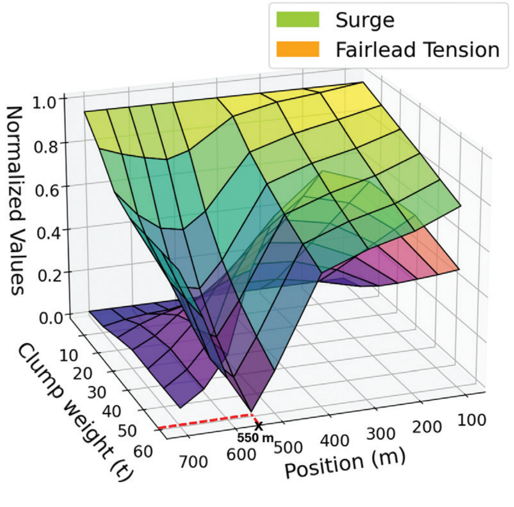

Fig. 8. 3D plot of fairlead tension and surge variation.

Simultaneously, a vector of candidate memory values $\widehat{\mathbf{c}}_t$ is computed using an tanh activation function:

$$\widehat{\mathbf{c}}_t = \tanh\left(\mathbf{W}_c[\mathbf{h}_{t-1}\ \mathbf{x}_t] + \mathbf{b}_c\right) \tag{7}$$

The updated memory cell $\mathbf{c}_t$ is then obtained by combining the contributions of the previous memory cell and the candidate values, modulated by their respective gates:

$$\mathbf{c}_t = \mathbf{f}_t \circ \mathbf{c}_{t-1} + \mathbf{i}_t \circ \widehat{\mathbf{c}}_t \tag{8}$$

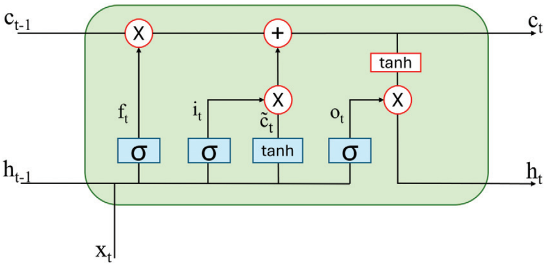

Fig. 9. LSTM unit.

Here, the operator ∘ denotes element-wise multiplication. The output gate $\mathbf{o}_t$ controls which information from the memory cell is exposed to the next layer or the subsequent time step:

$$\mathbf{o}_t = \sigma(\mathbf{W}o[\mathbf{h}_{t-1}\ \mathbf{x}_t] + \mathbf{b}_o) \tag{9}$$

Finally, the hidden state, which also serves as the output of the LSTM cell at time t, is computed as:

$$\mathbf{h}_t = \mathbf{o}_t \circ \tanh(\mathbf{c}_t) \tag{10}$$

This gating mechanism allows LSTM cells to adaptively remember and forget information, making them particularly well suited for modeling complex temporal dependencies in data.

In this study, input to the LSTM model is denoted as $\mathbf{x}^d$, where d represents the number of distinct features, and each feature is observed over a time sequence of length T. Consequently, the input to each LSTM layer is a matrix of dimensions $T \times d$, where T is the number of time steps and d is the number of features. For any time step, t the output h_t from the LSTM layer is given as:

$$\{\mathbf{h_t}; \mathbf{c_t}\} = \mathrm{LSTM}(\{\mathbf{h_{t-1}}; \mathbf{c_{t-1}}\}) \tag{11}$$

The LSTM processes the sequence and generates a hidden state $\mathbf{h}_T$ at the final time step, which encapsulates the temporal information learned from the sequence. This final hidden state is passed through a fully connected (dense) output layer, followed by a softmax activation function to produce the class probability distribution, denoted by $\hat{\mathbf{y}}$:

$$\hat{\mathbf{y}} = \mathrm{softmax}(\mathbf{W}_y\mathbf{h}_T + \mathbf{b}_y) \tag{12}$$

where $\mathbf{W}_y$ and $\mathbf{b}_y$ are the weights and biases of the output layer, respectively.

The model is trained to minimize the prediction error using the categorical cross-entropy loss function, defined as:

$$\mathcal{L}_{\mathrm{CE}} = -\frac{1}{N}\sum_{i=1}^{N}\sum_{c=1}^{C} y_c^{(i)} \log \hat{y}_c^{(i)} \tag{13}$$

where N is the number of training samples, C is the number of classes, $\hat{y}_c^{(i)}$ is the predicted probability for class c on the i-th sample, and $y_c^{(i)}$ is the corresponding one-hot encoded ground truth.

IV. CLUMP WEIGHT LOSS DETECTION

The proposed DL method is trained on a simulated dataset generated using the OC3 FOWT model within the OpenFAST simulation framework. This section provides an overview of the simulation setup and details the input features selection to train the LSTM model.

A. SELECTION OF INPUT FEATURES

To determine the responses most influenced by wind and wave forces, the Pearson correlation coefficient (r) is utilized. This coefficient quantifies the strength and direction of the linear association between two continuous variables, taking values between −1 and +1. A positive value of r suggests a direct relationship, meaning both variables increase together, while a negative value indicates an inverse relationship—where one variable increases as the other decreases. An r value of zero signifies the absence of a linear correlation. The expression for computing r is defined as:

$$r = \frac{\sum_{i=1}^{n}(X_i - \bar{X})(Y_i - \bar{Y})}{\sqrt{\sum_{i=1}^{n}(X_i - \bar{X})^2}\sqrt{\sum_{i=1}^{n}(Y_i - \bar{Y})^2}} \tag{14}$$

where X_i, Y_i are the data points and $\overline{X}, \overline{Y}$ are their respective means. The coefficient is dimensionless and classifies the strength of the correlation as weak, moderate, or strong based on its magnitude.

Figure 10 illustrates the Pearson correlation matrix for different features of the floating platform. The correlation coefficients between wave elevation and the 6-*DOF* platform responses have been shown in Fig. 11. Features were selected based on the absolute value of the correlation coefficient $|r|$, as both positive and negative correlations indicate strong linear relationships. Accordingly, surge, heave, and pitch—having the largest $|r|$ values—were chosen as input features for the LSTM model, while sway, roll, and yaw, with $|r|$ values close to zero, were excluded.

B. SIMULATIONS

The simulation data were generated from the OC3 turbine model, incorporating eight different scenarios of clump weight loss as shown in Table IV, where (×) indicates a detached clump weight and (∘) represents an attached one.

The simulations were carried out under varying environmental loading conditions, as summarized in Table V. Wave heights ranged from 4 to 6 meters in 1-meter

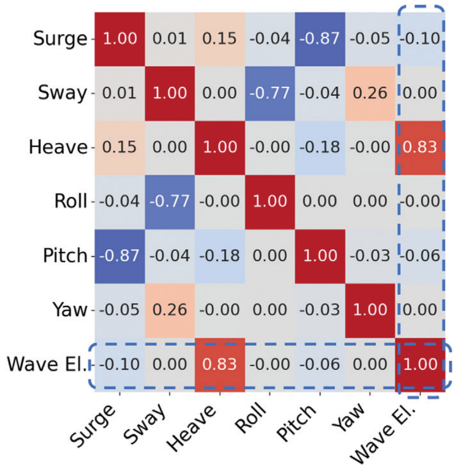

	Surge	Sway	Heave	Roll	Pitch	Yaw	Wave El.
Surge	1.00	0.01	0.15	-0.04	-0.87	-0.05	-0.10
Sway	0.01	1.00	0.00	-0.77	-0.04	0.26	0.00
Heave	0.15	0.00	1.00	-0.00	-0.18	-0.00	0.83
Roll	-0.04	-0.77	-0.00	1.00	0.00	0.00	-0.00
Pitch	-0.87	-0.04	-0.18	0.00	1.00	-0.03	-0.06
Yaw	-0.05	0.26	-0.00	0.00	-0.03	1.00	0.00
Wave El.	-0.10	0.00	0.83	-0.00	-0.06	0.00	1.00

Fig. 10. Pearson's correlation matrix for wave elevation and different responses of the floating platform.

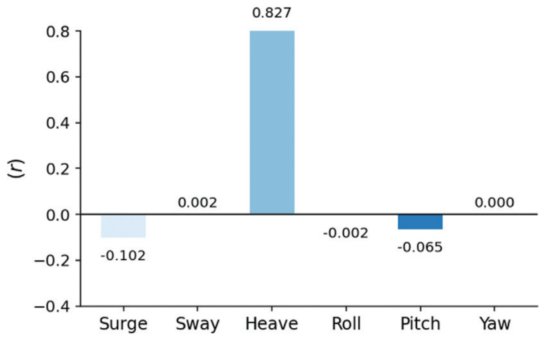

Fig. 11. Pearson's correlation coefficients for 6-*DOF* of the floating platform due to wave elevation.

Table IV. Attached clump weight in different cases

Case	Line 1	Line 2	Line 3
$\mathcal{C}_0$	×	×	×
$\mathcal{C}_1$	∘	×	×
$\mathcal{C}_2$	×	∘	×
$\mathcal{C}_3$	×	×	∘
$\mathcal{C}_{12}$	∘	∘	×
$\mathcal{C}_{23}$	×	∘	∘
$\mathcal{C}_{13}$	∘	×	∘
$\mathcal{C}_{123}$	∘	∘	∘

Table V. Environmental loadings for OpenFAST simulations

H_s	T_p	Wind	Direction
$4-6\,\mathrm{m}$	$8-9\,\mathrm{s}$	$9-12\,\mathrm{m/s}$	$-30°$ to $30°$

intervals, while wave periods varied between 8 and 9 seconds. Wind speeds were set between 9 and 12 m/s with 1 m/s increments. Additionally, the loading direction was varied from $-30°$ to $30°$ in steps of $15°$ (C.f. Fig. 3).

For each wind and wave direction, in total 50 simulations were performed to capture different wave realizations. For each case listed in Table IV, approximately 250 simulations were conducted for 5 different directions. In total, 2000 simulations were carried out across eight distinct clump weight configurations.

C. DATA PREPROCESSING

The raw time-series data from these 2000 simulations were sampled at 40 Hz, giving 1200 s of data per run. The initial 600 s were discarded to eliminate transient effects, leaving 600 s of steady-state response per simulation. Each record was then divided into non-overlapping windows of 200 time steps, equivalent to 5 s of motion data, resulting in 120 sequences per simulation and a total of 240,000 labeled sequences across all cases. The three platform motions—surge, heave, and pitch—were retained as features and reshaped into sequences of size (200×3) for input to the LSTM. The output labels corresponding to clump weight configurations were converted into one-hot encoded vectors for classification. Although min–max normalization was tested during preliminary experiments, the raw sequences were used directly in training since normalization did not provide a noticeable performance improvement. No additional data augmentation was performed.

D. LSTM TRAINING

To train the LSTM model, three input features—surge, heave, and pitch—were extracted from the simulated platform motion data. A single-layer LSTM architecture with a single dense hidden layer was adopted for this study. The optimal number of neurons in the LSTM layer was determined through a performance evaluation in which the smallest sequence length of 40 (i.e. 1 second) was held constant while the number of neurons was varied for 50 epochs each. As illustrated in Fig. 12, the architecture with 256 neurons provided the best performance in terms of cross-entropy loss while having low training time and was therefore selected for the final model configuration. In addition to the number of LSTM units, the impact of different activation functions was also evaluated to assess the robustness of the model. The results showed that the ReLU and *tanh* functions achieved the highest performance (86%), followed by the sigmoid function (84%). Consequently, the ReLU activation function was adopted in this study.

Although LSTM networks are capable of retaining sequential dependencies, their effectiveness is limited by sequence length due to memory constraints. Therefore, an appropriate sequence length was determined through a sensitivity analysis, as illustrated in Fig. 13. In this test, a single-layer 256-unit LSTM architecture with fixed hyperparameters was trained for 50 epochs across various sequence lengths. The results indicate that a sequence length of 200 (i.e. 5 seconds) provides a suitable balance between performance and efficiency for this study.

The dataset was divided into 80% for training, 10% for validation, and 10% for testing the LSTM-based clump weight monitoring model. The split was random after shuffling to ensure robust training and to avoid overfitting. The architecture of the LSTM model is summarized in Table VI. The model was developed in Python using the TensorFlow Keras library [37]. The training and validation loss curves are shown in Fig. 14, which demonstrates that the model trained effectively without signs of overfitting or underfitting throughout the training process.

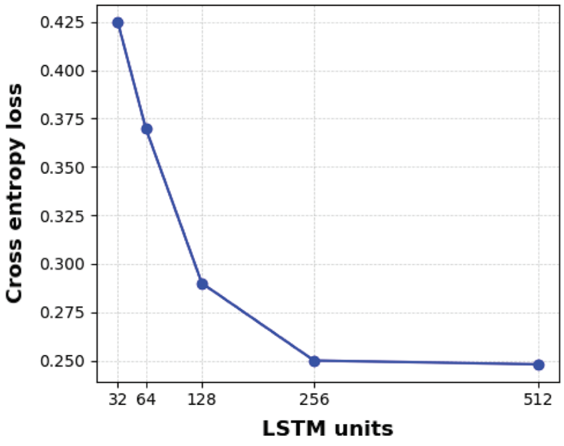

Fig. 12. Cross-entropy loss for different LSTM units.

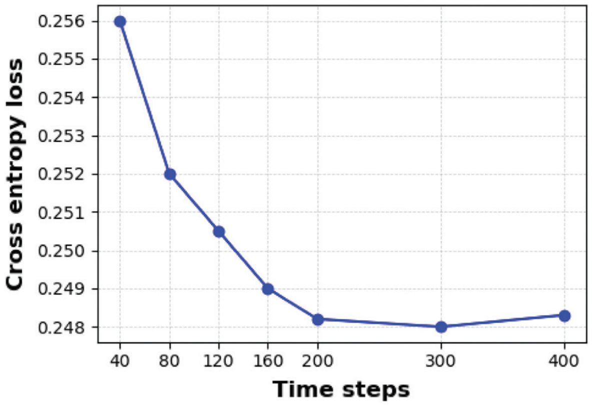

Fig. 13. Cross-entropy loss for different input sequence lengths.

Table VI. The architecture of the LSTM model

LSTM architecture		
Layer	**Activation function**	**Units**
Input shape	–	(400.3)
LSTM	–	256
Dense	Relu	1024
Output layer	softmax	8
Hyperparameters		
Optimizer		Adam
Epochs		200
Learning rate		10^{-5}
Training time		
System	Intel i7, 16 GB DDR4 RAM	
Time per epoch		10 min
Total time		2000 min

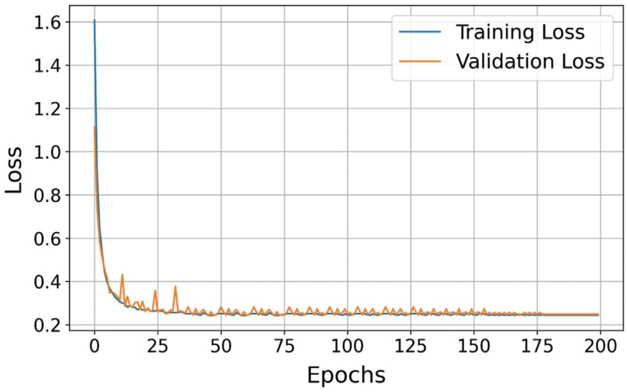

Fig. 14. Training and validation loss curve.

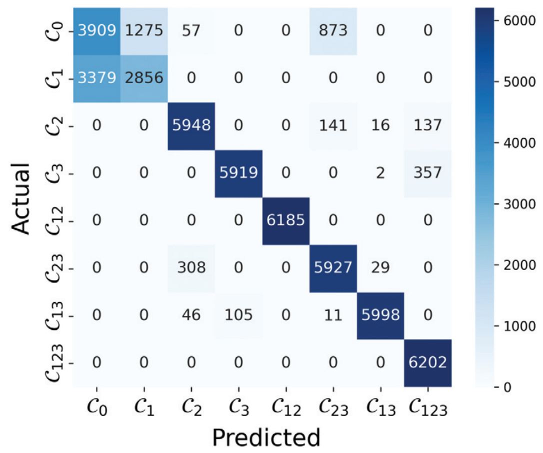

	$\mathcal{C}_0$	$\mathcal{C}_1$	$\mathcal{C}_2$	$\mathcal{C}_3$	$\mathcal{C}_{12}$	$\mathcal{C}_{23}$	$\mathcal{C}_{13}$	$\mathcal{C}_{123}$
$\mathcal{C}_0$	3909	1275	57	0	0	873	0	0
$\mathcal{C}_1$	3379	2856	0	0	0	0	0	0
$\mathcal{C}_2$	0	0	5948	0	0	141	16	137
$\mathcal{C}_3$	0	0	0	5919	0	0	2	357
$\mathcal{C}_{12}$	0	0	0	0	6185	0	0	0
$\mathcal{C}_{23}$	0	0	308	0	0	5927	29	0
$\mathcal{C}_{13}$	0	0	46	105	0	11	5998	0
$\mathcal{C}_{123}$	0	0	0	0	0	0	0	6202

Fig. 15. Confusion matrix for clump weight loss classification.

Table VII. Classification report showing precision, recall, and F1-score for each case

Case	**Precision**	**Recall**	**F1-score**
$\mathcal{C}_0$	0.54	0.64	0.58
$\mathcal{C}_1$	0.69	0.46	0.55
$\mathcal{C}_2$	0.94	0.95	0.94
$\mathcal{C}_3$	0.98	0.94	0.96
$\mathcal{C}_{12}$	1.00	1.00	1.00
$\mathcal{C}_{23}$	0.85	0.95	0.90
$\mathcal{C}_{13}$	0.99	0.97	0.98
$\mathcal{C}_{123}$	0.93	1.00	0.96

The model was evaluated on the test dataset, yielding an average MSE of 0.2404 and an accuracy of 86%. The confusion matrix for the testing dataset, which includes eight clump weight configurations ($\mathcal{C}_0$ to $\mathcal{C}_{123}$), is presented in Fig. 15.

High precision, recall, and F1-scores detailed in Table VII were achieved for all cases except $\mathcal{C}_1$ and $\mathcal{C}_0$. In several instances, the model misclassified $\mathcal{C}_0$ as $\mathcal{C}_1$, and vice versa. This misclassification is attributed to the highly similar platform dynamics exhibited by these two configurations. A Pearson correlation test between surge, heave, and pitch response for $\mathcal{C}_0$ and the other cases, presented in Table VIII, confirms this similarity. The correlation coefficient between $\mathcal{C}_0$ and $\mathcal{C}_1$ was found to be 1.0, indicating identical dynamic responses. This suggests that adding a clump weight to a single mooring line in the direction of wave and current does not significantly affect the platform's motion characteristics.

Furthermore, to evaluate the model's generalization ability, it was tested on an unseen dataset simulated under the loading conditions specified in Table IX. The reported 86% accuracy corresponds to the held-out test split, whereas evaluation on the completely unseen dataset generated under deviating environmental conditions resulted in a reduced accuracy of 73%. This distinction emphasizes the model's generalization capability, albeit with some loss of

Table VIII. Pearson's correlation between case $\mathcal{C}_0$ and other cases

	$\mathcal{C}_1$	$\mathcal{C}_2$	$\mathcal{C}_3$	$\mathcal{C}_{12}$	$\mathcal{C}_{23}$	$\mathcal{C}_{13}$	$\mathcal{C}_{123}$
$\mathcal{C}_0$	1.000	0.996	0.992	0.994	0.993	0.991	0.986

Table IX. Environmental loadings for unseen dataset

H_s	T_p	**Wind**	**Direction**
5 m	9 s	11 m/s	10°

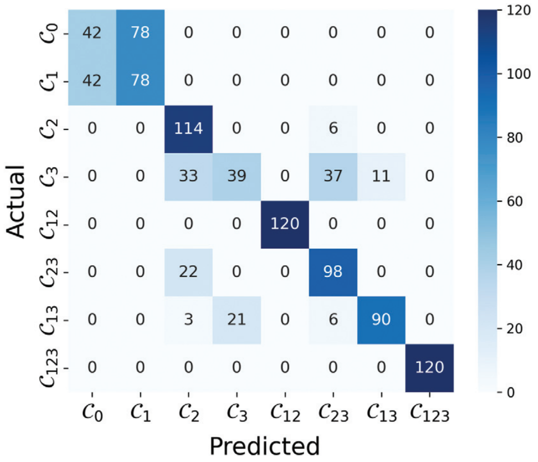

	C_0	C_1	C_2	C_3	C_{12}	C_{23}	C_{13}	C_{123}
C_0	42	78	0	0	0	0	0	0
C_1	42	78	0	0	0	0	0	0
C_2	0	0	114	0	0	6	0	0
C_3	0	0	33	39	0	37	11	0
C_{12}	0	0	0	0	120	0	0	0
C_{23}	0	0	22	0	0	98	0	0
C_{13}	0	0	3	21	0	6	90	0
C_{123}	0	0	0	0	0	0	0	120

Fig. 16. Confusion matrix for unseen dataset.

performance compared to the original distribution. The corresponding confusion matrix is presented in Fig. 16.

To further benchmark the proposed approach, additional models were implemented for comparison. In particular, ANN and convolutional neural network (CNN) baselines of similar complexity were trained on the same dataset using identical hyperparameters. The model architectures and classification accuracies are summarized in Table X. It is evident that the LSTM provides the highest accuracy.

These results clearly justify the choice of LSTM as the primary model in this study, given its superior performance in clump weight classification.

V. DISCUSSION

The overall performance of the proposed LSTM-based classifier highlights its effectiveness in detecting clump weight loss conditions in FOWTs using platform motion data. The model achieved high classification accuracy across most configurations and demonstrated robustness under varying environmental conditions. These findings underscore the feasibility of applying DL techniques for real-time SHM in offshore applications.

Despite its strong performance, the model frequently misclassified Case $\mathcal{C}_0$, with no clump weights as Case $\mathcal{C}_1$, where a clump weight remains on the mooring line. This misclassification likely results from the dynamic similarity between the two configurations. Consequently, the platform's global motion responses in Cases $\mathcal{C}_0$ and $\mathcal{C}_1$ have virtually identical response signatures, leading to consistent misclassification. This limitation stems not from the learning algorithm itself, but rather from the insufficient observability of clump weight loss when relying solely on global platform motion data. Thus, exclusive dependence on global motions (surge, heave, and pitch), which are practical and easily accessible, may not be sensitive enough to capture subtle differences in mooring line conditions. Incorporating localized responses, such as mooring line tension or fairlead acceleration, may offer additional discriminative features to enhance detection accuracy.

Furthermore, this study focuses on configurations involving a single clump weight. In practice, mooring systems may employ multiple clump weights depending on design requirements. Future work can extend this approach to accommodate multiple clump weights and more complex damage scenarios. Although the developed model achieves approximately 86% detection accuracy across cases, the use of more sensitive response variables and additional sensor inputs could further improve the robustness and precision of the DL framework. The application of AI in critical infrastructure such as offshore wind farms also raises ethical considerations. Key aspects include transparency of decision-making, accountability for errors, and ensuring that automated monitoring supports rather than replaces human oversight. These elements should be carefully addressed in future deployments of the proposed framework.

Building on these considerations, future work will focus on addressing practical deployment challenges. Sensor placement strategies must be optimized to ensure that both global platform motions and localized mooring responses are captured effectively. Reliable offshore-to-shore data transmission also needs to be ensured under bandwidth and latency constraints typical of marine environments. In addition, the LSTM model will require periodic retraining and updates to remain robust under evolving environmental conditions and long-term structural changes. Addressing these aspects will be essential for translating the proposed framework from simulation-based validation to real-world offshore wind applications.

VI. CONCLUSION

This study presents a DL framework for the real-time monitoring of mooring systems in FOWTs. An LSTM-based DL model was developed to detect clump weight loss scenarios using only platform motion responses. The model achieved an overall classification accuracy of 86% on the held-out test split and 73% on a completely unseen dataset, demonstrating both strong predictive capability and robustness under varying environmental loading directions.

While the model accurately identified most configurations, it faced challenges in distinguishing between the

Table X. Comparison of ANN, CNN, and LSTM models for clump weight classification

Parameter	ANN	CNN	LSTM
Model architecture	Input: 200 features Dense (256, ReLU) Dense (64, ReLU) Dense (8, Softmax)	Input: sequence (200,3) Conv1D (32, kernel=3, ReLU) MaxPooling1D (pool=2) Flatten Dense (64, ReLU) Dense (8, Softmax)	Input: sequence (200,3) LSTM (256 units) Dense (1024, ReLU) Dense (8, Softmax)
Accuracy	81%	79%	86%

complete clump weight loss scenario ($\mathcal{C}_0$) and the configuration with a single clump weight on mooring line 1 ($\mathcal{C}_1$), likely due to the dynamic similarity in platform responses between these two cases. Overall, the proposed approach highlights a promising pathway for real-time, data-driven SHM in offshore wind energy systems. This study also carries broader implications for renewable energy and offshore engineering. By applying a data-driven classification framework to FOWTs, it demonstrates how advanced ML methods can strengthen SHM practices. Such approaches can improve operational reliability, reduce maintenance costs, and extend the service life of offshore wind farms. In doing so, this work contributes to the long-term sustainability and resilience of renewable energy infrastructure, supporting the global transition toward cleaner energy systems.

CONFLICT OF INTEREST STATEMENT

The authors declare no conflicts of interest.

REFERENCES

[1] R. James and M. C. Ros, "Floating offshore wind: Market and technology review," *Carbon Trust*, 2015.

[2] S. Rui *et al.*, "A review on mooring lines and anchors of floating marine structures," *Renew. Sustain. Energy Rev.*, vol. 199, p. 114547, 2024.

[3] E. Fontaine *et al.*, "Industry survey of past failures, pre-emptive replacements and reported degradations for mooring systems of floating production units," in *Offshore technology conference*. OTC, 2014, p. D041S047R002.

[4] K.-T. Ma *et al.*, "A historical review on integrity issues of permanent mooring systems," in *Offshore Technology Conference*. OTC, 2013, pp. OTC–24 025.

[5] H. Li, H. Diaz, and C. Guedes Soares, "A developed failure mode and effect analysis for floating offshore wind turbine support structures," *Renew. Energy*, vol. 164, pp. 133–145, 2021.

[6] N. Bruschi *et al.*, "Influence of clumps-weighted moorings on a spar buoy offshore wind turbine," *Energies*, vol. 13, no. 23, p. 6407, 2020.

[7] J. Li *et al.*, "Study on the mooring systems attaching clump weights and heavy chains for improving the typhoon resistance of floating offshore wind turbines," *Ocean Eng.*, vol. 311, p. 118734, 2024.

[8] J. Ding *et al.*, "Influence of mooring clump weight on the dynamic responses of a floating offshore wind turbine located in shallow water," in *Proceedings of 10th International Conference on Coastal and Ocean Engineering*, D.-S. Jeng and D. Wan, Eds. Singapore: Springer Nature Singapore, 2024, pp. 104–118.

[9] Q. Pan, M. Y. Mahfouz, and F. Lemmer, "Assessment of mooring configurations for the iea 15mw floating offshore wind turbine," *J. Phys. Conf. Ser.*, vol. 2018, no. 1, p. 012030, Sep. 2021.

[10] J. Chen *et al.*, "Sensitivity analysis of mooring chain fatigue of floating offshore wind turbines in shallow water," *J. Mar. Sci. Eng.*, vol. 12, no. 10, Art. no. 1807, 2024.

[11] K. T. Ma *et al.*, *Mooring System Engineering for Offshore Structures*. Oxford, UK: Gulf Professional Publishing, 2019. [Online]. Available: https://books.google.co.in/books?id=Bx2bDwAAQBAJ.

[12] *Mooring Designs for Floating Offshore Wind Turbines Leveraging Experience From the Oil & Gas Industry*, ser. International Conference on Offshore Mechanics and Arctic Engineering, vol. 1: Offshore Technology, 06 2021.

[13] J. Zhang and X. Wang, "Identification of lost clump weights and real-time prediction of mooring line top-tension," *J. Offshore Mech. Arct. Eng.*, vol. 145, no. 3, p. 031701, 2023.

[14] M. Chung *et al.*, "Detection of damaged mooring line based on deep neural networks," *Ocean Eng.*, vol. 209, p. 107522, 2020.

[15] N. Gorostidi, D. Pardo, and V. Nava, "Diagnosis of the health status of mooring systems for floating offshore wind turbines using autoencoders," *Ocean Eng.*, vol. 287, p. 115862, 2023.

[16] R. Kumar *et al.*, "Characterizing damage in wind turbine mooring using a data-driven predictor model within a particle filtering estimation framework," *PHM Soc. Eur. Conf.*, vol. 8, no. 1, p. 8, 2024.

[17] R. Kumar, S. Sen, and A. Keprate, "Real-time fatigue assessment of floating offshore wind turbine mooring employing sequence-to-sequence-based deep learning on indirect fatigue response," *Ocean Eng.*, vol. 315, p. 119741, 2025.

[18] H.-C. Kim, M.-H. Kim, and D.-E. Choe, "Structural health monitoring of towers and blades for floating offshore wind turbines using operational modal analysis and modal properties with numerical-sensor signals," *Ocean Eng.*, vol. 188, p. 106226, 2019.

[19] A. Thakur *et al.*, "Integrating dl-based surrogate within an interacting particle ensemble kalman filtering framework for computationally efficient condition monitoring of fowt moorings," *Ocean Eng.*, vol. 330, p. 121223, 2025.

[20] R. Kumar *et al.*, "Addressing material uncertainty in reliability analysis of floating offshore mooring through probabilistic meta-model developed with stochastic kriging technique," *Ocean Eng.*, vol. 335, p. 121697, 2025.

[21] N. Gorostidi *et al.*, "Predictive maintenance of floating offshore wind turbine mooring lines using deep neural networks," *J. Phys. Conf. Ser.*, vol. 2257, IOP Publishing, p. 012008, 2022.

[22] K. Tandon and S. Sen., "A probabilistic integration of lstm and gaussian process regression for uncertainty-aware reservoir water level predictions," *Hydrol. Sci. J.*, vol. 70, no. 1, pp. 144–161, 2025.

[23] J. Jia and Y. Li, "Deep learning for structural health monitoring: Data, algorithms, applications, challenges, and trends," *Sensors*, vol. 23, no. 21, p. 8824, 2023.

[24] H. Wan *et al.*, "A novel transformer model for surface damage detection and cognition of concrete bridges," *Expert Syst. Appl.*, vol. 213, p. 119019, 2023.

[25] S. Deng, D. Ning, and R. Mayon, "The motion forecasting study of floating offshore wind turbine using self-attention long short-term memory method," *Ocean Eng.*, vol. 310, p. 118709, 2024. [Online]. Available: https://www.sciencedirect.com/science/article/pii/S002980182402047X

[26] D.-E. Choe, H.-C. Kim, and M.-H. Kim, "Sequence-based modeling of deep learning with lstm and gru networks for structural damage detection of floating offshore wind turbine blades," *Renew. Energy*, vol. 174, pp. 218–235, 2021.

[27] T. Das and S. Guchhait, "A hybrid gru and lstm-based deep learning approach for multiclass structural damage identification using dynamic acceleration data," *Eng. Fail. Anal.*, vol. 170, p. 109259, 2025.

[28] E. Sadeghian, E. Dragomirescu, and D. Inkpen, "Damage detection for a cantilevered steel i-beam through deep-learning methods: Lstm, multivariate time-series transformer, and lstm-based autoencoder," *J. Comput. Civil Eng.*, vol. 39, no. 2, p. 04025003, 2025.

[29] J. Jonkman, “Definition of the floating system for phase iv of oc3,” National Renewable Energy Laboratory (NREL), Technical Report NREL/SR-500-47535, 2010. [Online]. Available: https://www.nrel.gov/docs/fy10osti/47535.pdf.

[30] B. Jonkman *et al.*, “Openfast/openfast: Openfast v3.1.0,” Mar. 2022.

[31] NREL, *OpenFAST Documentation*, 2023. [Online]. Available: https://openfast.readthedocs.io/en/main/.

[32] V. Piscopo *et al.*, “Fatigue assessment of moorings for floating offshore wind turbines by advanced spectral analysis methods,” *J. Mar. Sci. Eng.*, vol. 10, no. 1, Art. no. 37, 2021.

[33] K. Hasselmann *et al.*, “Measurements of wind-wave growth and swell decay during the joint north sea wave project (jonswap),” *Dtsch. Hydrodynamik*, vol. 1, pp. 1–75, 1973.

[34] T. Burton *et al.*, *Wind Energy Handbook*, 2nd ed. Chichester, UK: John Wiley & Sons, 2011.

[35] J. Jonkman and W. Musial, “Offshore Code Comparison Collaboration (OC3) for IEA Task 23 Offshore Wind Technology and Deployment,” National Renewable Energy Laboratory (NREL), Golden, Colorado, Tech. Rep. NREL/SR-500-48191, 2007. [Online]. Available: https://www.nrel.gov/docs/fy08osti/48191.pdf.

[36] Y. Yu *et al.*, “A review of recurrent neural networks: Lstm cells and network architectures,” *Neural Comput.*, vol. 31, no. 7, pp. 1235–1270, 07 2019.

[37] M. Abadi *et al.*, “TensorFlow: Large-scale machine learning on heterogeneous systems,” 2015, software available from tensorflow.org. [Online]. Available: http://tensorflow.org/.